Improving the field homogeneity of fixed- and variable-diameter discrete Halbach magnet arrays for MRI via optimization of the angular magnetization distribution

Tewari, S.; O'Reilly, T.; Webb, A.

Journal of Magnetic Resonance 324 (2021) 106923

Contents lists available at ScienceDirect

Journal of Magnetic Resonance

journal homepage: www.elsevier.com/locate/jmr

Communication

Improving the field homogeneity of fixed- and variable-diameter discrete Halbach magnet arrays for MRI via optimization of the angular magnetization distribution

Sumit Tewari, Thomas O'Reilly, Andrew Webb *

C.J. Gorter Center for High-Field MRI, Leiden University Medical Center, Department of Radiology, Albinusdreef 2, 2333 ZA Leiden, The Netherlands

ARTICLE INFO

Article history:
Received 1 November 2020
Revised 5 January 2021
Accepted 18 January 2021
Available online 27 January 2021

Keywords:
Halbach configuration
MRI
Finite-length magnets
Magnetization orientation
Random-search

ABSTRACT

The aim of this work was to maximize the homogeneity of fixed- or variable-diameter Halbach array of discrete magnets by optimizing the angular rotation of individual magnets within each ring of the array. Numerical simulations have been performed for magnet arrays with various length:radius ratios (L/R) using a dipole-approximation model. These simulations used an uninformed random-search algorithm, with the initial state corresponding to the classical Halbach dipole configuration. Two different classes of systems were studied, one with magnet rings of constant radius, and the other in which the radius of the rings was allowed to vary to increase the homogeneity. Simulation results showed that for a fixed-diameter array optimization of the angular orientation of individual magnets increased the homogeneity by ~17% for very short magnets, with the improvement dropping to ~5% for L/R values greater than ~3:1, where the homogeneity was measured over a region-of-interest equal to one-half the diameter of the magnet array. An empirical formula was derived which allows easy estimation of the required magnetization angles for any L/R. For a 23-ring variable diameter magnet with L/R of ~4:1 the optimization procedure produces an increase in homogeneity of ~18%.

1. Introduction

Halbach magnet arrays, first described in the 1970s [1–4], have found a wide range of applications including electrical motors [5], magnetic refrigeration [6], energy harvesting [7], and undulators [8], due to their ability to efficiently generate specific rotationally-symmetric magnetic field distributions. Cylindrical Halbach arrays, arranged in the so-called dipole configuration, have been of particular interest for NMR and MRI. In this configuration the orientation of the magnetisation rotates as the sinusoid of twice the azimuthal angle (θ) generating a strong and homogeneous radially-oriented magnetic field inside the cylinder, and zero field outside the magnet for infinitely long configurations. Following the nomenclature of Hilton [9] the magnetization $\boldsymbol{M}$ varies with angular position θ:

$$\boldsymbol{J}(\theta) = \mu_0 \boldsymbol{M}(\theta) = \boldsymbol{B}_r\{sin(2\theta)\hat{\boldsymbol{x}} - cos(2\theta)\hat{\boldsymbol{y}}\} \quad [1]$$

where μ_0 is the permeability of free space, $\boldsymbol{J}$ is the magnetic polarization, and $\boldsymbol{B}_r$ is the remanent flux density. The x,y plane is perpendicular to the long-axis of the magnet (denoted z): the overall geometric configuration is shown schematically in Fig. 1. This configuration produces a magnetic field $\boldsymbol{B}$ given by [4] :

$$\boldsymbol{B} = B_r ln\left(\frac{r_{out}}{r_{inn}}\right)\hat{\boldsymbol{y}} \quad [2]$$

where r_{out} and r_{inn} are the outer and inner radii of the cylinder, respectively.

For NMR and MRI applications, a key factor is the magnetic field homogeneity over the sample or imaging region-of-interest (ROI). In real-world systems the magnetic field homogeneity is significantly lower than its theoretical maximum due to intrinsic end-effects caused by the finite length of the system [10,11] and the use of discrete magnets to approximate the continuous magnetisation distribution [12,13], which also reduces the value of $\boldsymbol{B}$. If the magnet is segmented into n sections, each with magnetization equal to that of the continuous Halbach cylinder at the centre of each section, then the magnitude of the magnetic field, compared to that in Eq. [2], is reduced to [11]:

$$B(n) = B_\infty \frac{sin\left(\frac{2\pi}{n}\right)}{\left(\frac{2\pi}{n}\right)} \quad [3]$$

* Corresponding author.
E-mail address: a.webb@lumc.nl (A. Webb).

https://doi.org/10.1016/j.jmr.2021.106923
1090-7807/

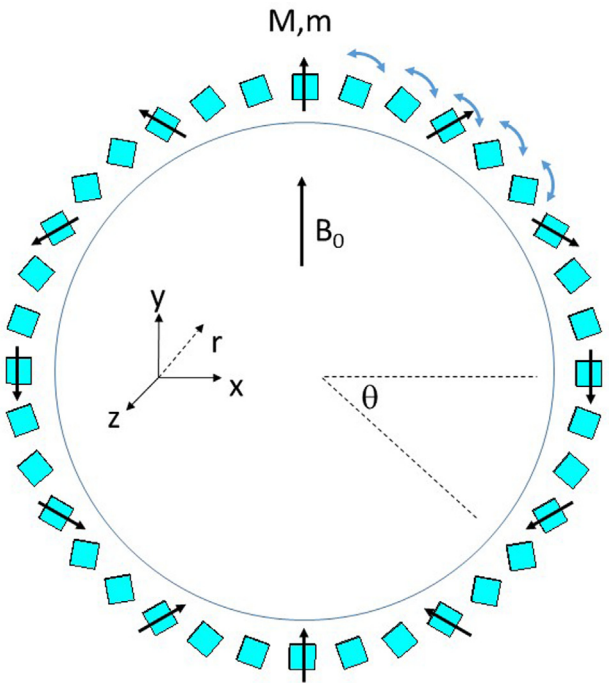

Fig. 1. Schematic showing the geometry and nomenclature used for the Halbach array. θ is the azimuthal angle, and the magnetic field B_0 is calculated at each point r via the summation of the fields from each individual magnet, derived from a dipole-approximation model. Optimization of the field homogeneity involves rotations of each of the magnets within the plane, as indicated by the double-headed blue arrows. (For interpretation of the references to colour in this figure legend, the reader is referred to the web version of this article.)

For the majority of low-field NMR and MRI magnets, the so-called "Mandhala" (magnet arrangements for novel discrete Halbach layout) is used for design and construction, in which a large number of discrete, typically cubic or rectangular (cylindrical has also been shown) magnets are used: the topic was the subject of a recent comprehensive review article [14].

For most practical systems the finite length of the Halbach cylinder causes the most significant perturbations to the ideal dipolar magnetic field, and these perturbations increase as the length-to-radius ratio (L/R) of the magnet becomes smaller [11]. A number of studies of increasing mathematical complexity analyzing the magnet homogeneity have been published. Simple analyses of magnets with high aspect ratios (in which a 2D description can be used) were initially presented by Halbach [2–4], in which the end effects were not considered. The effects of segmentation were shown in 2D to disturb the field homogeneity by producing harmonics of orders equal to multiples of the total number of segments [2]. Three-dimensional models of finite aspect ratio magnets were then derived [10,15,16], as well as using a simple dipole approximation to analyze very short systems [13], and spherical harmonic expansions of the scalar potential and magnetic field have been used to design simple permanent magnet assemblies [17]. Ni Mhiochain et al. [10] studied the main sources of magnet inhomogeneity in finite length, segmented magnets in order to estimate the torque between two nested magnet arrays: in the case of infinite length unsegmented arrays the torque would be zero. They showed that the inhomogeneity term, △B, along the axis was a function of L/R. Turek and Liszkowski [11] have presented the most comprehensive mathematical analysis of the effects of finite length and segmentation of dipole Halbach magnets. They demonstrated analytically solvable equations capable of very high (~1 ppm) accuracy in the central volume of the magnet. They also showed that, if the area very close to the inner bore of the magnet is excluded from the analysis, then the segmentation-induced perturbations in 3D are well-described by the same equations as derived by Halbach for the infinite length case. Their work concluded that homogeneity suitable for MRI could be reached for a L/R greater than ~4:1, and so for ratios less than this then some form of compensation is necessary.

Several strategies have been used to compensate for the finite length, typically focusing on increasing the effective magnetisation density towards the ends of the Halbach cylinder or decreasing the spacing between individual ring segments [13,18]: an alternative approach of sparsifying the Halbach array by optimising the removal of individual magnets in the array [19] has also been demonstrated. Anferova et al. [20] showed that introducing a larger inter-ring distance at the centre of the magnet, together with a slight shift outwards of the magnets at 0°, 90°, 180° and 270° increased the homogeneity significantly: similar results were reported by Danieli et al. [21,22]. An alternative approach is to reduce the diameter of the cylinder towards the ends [9,19,23–27]. Hilton and McMurry [9] considered a linear decrease in diameter from the centre towards the end of the magnet, and optimized the slope of this decrease in order to maximize the homogeneity. In the extreme case the diameter tapers to zero at one end, producing the so-called test tube magnet [25]. Hu et al. [28] designed a small magnet for the human finger with 11 rings of eight trapezoidal magnets, with both the outer and inner diameters of the magnets optimized to increase the homogeneity.

Another approach, shown by Kustler, involves changing the individual magnet orientations to improve the magnetic field strength and homogeneity [29]. This work was performed on an Halbach magnet of one fixed length and bore size for a single-ring magnet structure with 16 trapezoidal shaped segments and the magnetization angles were varied for the non-polar magnets, i.e. the magnetization at 0°, 90°, 180° and 270° were fixed. Values of magnetization angles for the intermediate magnets were found to be 144°, 194° and 232° compared to the traditional Halbach values of 135°, 180° and 225°.

Here, we extend the work of Kustler [29] to an empirical investigation of optimizing magnetization angles over a large range of L/R values of Halbach arrays using cubic magnets. This work analyzes arrays with either fixed ring diameters, or variable diameters which can be used to increase the homogeneity. A random-search algorithm is used to derive empirical formulae which can be used to calculate magnetisation configurations for maximum homogeneity.

2. Methods

As illustrated in Fig. 1, the magnetic field at each point in the desired ROI is calculated using a dipole-approximation, where each NdBFe-(neodymium boron iron) magnet (a cube of dimensions $12 \times 12 \times 12$ mm^3) is simulated as a closed current loop [30]and its corresponding magnetic field is given as :

$$\boldsymbol{B}(\boldsymbol{r}) = \frac{\mu_0}{4\pi}\frac{1}{r^3}\left[3\hat{\boldsymbol{r}}(\boldsymbol{m}\cdot\hat{\boldsymbol{r}})\hat{r} - \boldsymbol{m}\right] \quad (4)$$

where $\boldsymbol{m}$ is the magnetic dipole moment of the individual NdBFe-magnets and $\boldsymbol{r}$ is the position vector where the magnetic field is calculated. Such dipole-approximations are computationally very efficient. Compared to using a full analytical solution for the 3D magnetic field for a cubic magnet derived by Engel-Herbert et al. [31], the errors are very small for a region-of-interest which is not extremely close to the magnet [30]: supplementary Figure S1 shows results comparing the two approaches.

For the "zero-length" case, i.e. a single magnet ring, a 2D version of the above expression was used, while for the multi-ring cases the full 3D expression was used. The diameter of the smallest ring in the array was set to be 270 mm to correspond to systems used for brain imaging [26]. Each magnet has a remanence of 1.3 Tesla. The gap between the individual rings of magnets is fixed at 22 mm. All simulations were performed at 5 mm spatial resolution. The ROI is given by a circle with diameter 50% of the inner diameter in the zero-length case, and a spherical volume with 50% of the diameter otherwise.

Simulations used an uninformed random-search algorithm which starts with magnets in each ring arranged in the conventional 2θ configuration. The algorithm generates random states around this starting point with magnetization vectors rotated within a ± 5° limit until it finds a new state which satisfies a simultaneous decrease in inhomogeneity defined as (maximum-minimum)/(mean). Once such a new state is found, it is set as a new starting state and the algorithm initiates a new search around this state. The algorithm is run until asymptotic convergence has been achieved.

3. Results

Fig. 2 shows the results of the random search algorithm for the zero-length Halbach array with a single-ring comprising of 36 NdBFe-magnets. Fig. 2(a) shows the convergence curve for the inhomogeneity values. The start and end states are marked by arrows, with the end state showing almost 32% lower inhomogeneity than the initial 2θ angular configuration. Fig. 2(b) shows the optimized magnet angles (open circles). Fig. 2(c)-(d) show the two-dimensional magnetic fields produced by the starting and ending states, with Fig. 2(e) illustrating the difference between the two states.

If we denote the angle of the magnetization of each magnet to be Ξ_M, then the straight line in Fig. 2(b) can be represented by the angular configuration of an infinite length Halbach array, namely:

$$\Xi_M^{\infty}(\theta) = 2\theta \quad [5]$$

For the zero-length single ring configuration corresponding to the the end-state shown Fig. 2(b), there is an additional term which can be fitted very well (solid orange line) to an additional term in cos(2θ):

$$\Xi_M^{0}(\theta) = 2\theta + \alpha cos(2\theta) \quad [6]$$

where α is a coefficient empirically determined to be ~π/8 rad (22.5°) for the zero-length configuration.

The situation for a finite length Halbach can also be represented by Eq. [6] with α having a value between the two extremes of 0 (infinite length) and π/8 (single ring). Since it is expected that the value of α depends on the L/R of the array, simulations were performed for a range of values in order to determine the optimum values of α for maximum homogeneity: the results are shown in Fig. 3.

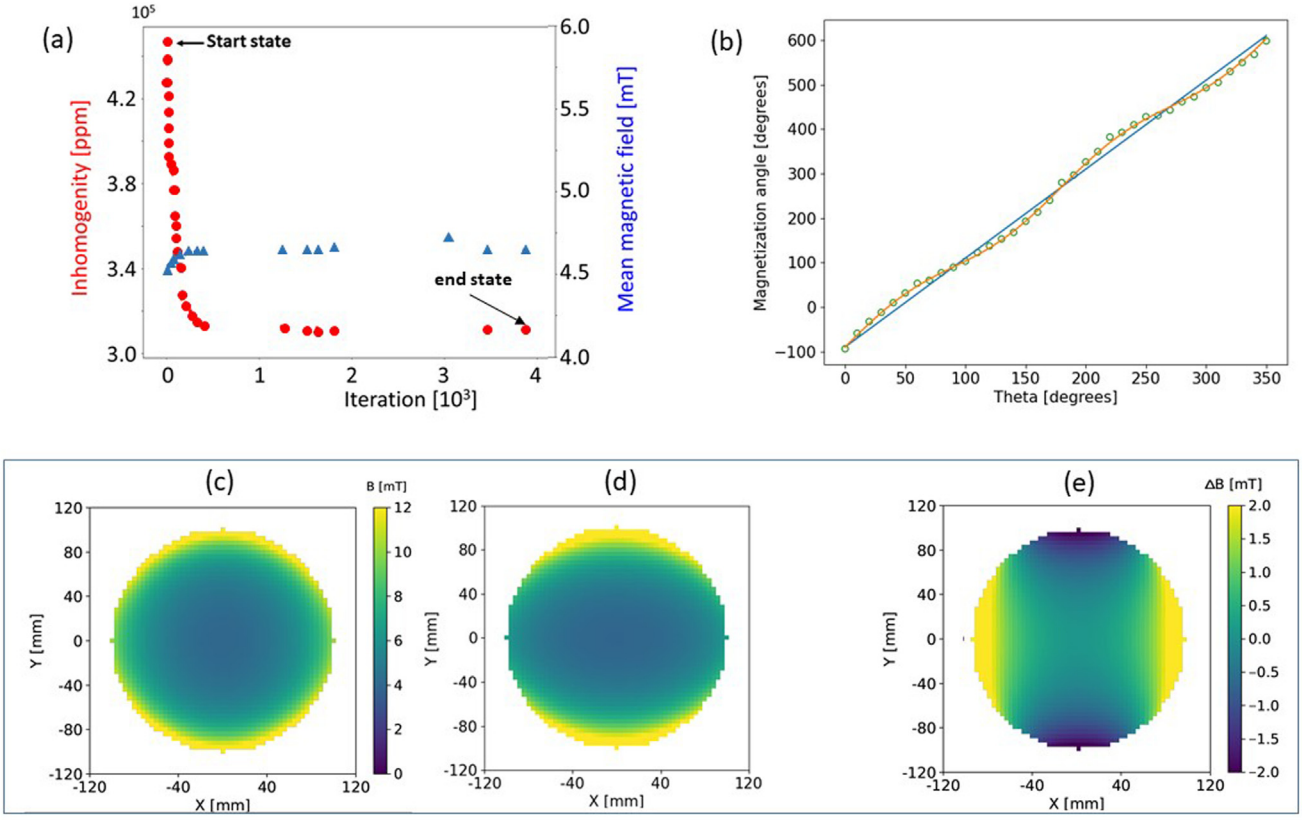

Fig. 2. (a) Convergence of the random-search algorithm to an end-state for a zero-length Halbach system (diameter = 270 mm), plotting inhomogeneity and mean magnetic field as a function of iteration number. (b) Plot of the angular rotation of each magnet with the starting-state being the conventional 2θ variation shown by the solid blue line The end-state is shown by the green open circles, together with a fit (solid orange line) integrating an additional cos(2θ) dependence – see Eq. [6]. (c) A plot of the magnetic field for the start state, (d) corresponding plot for the end state and (e) difference between start and end states. (For interpretation of the references to colour in this figure legend, the reader is referred to the web version of this article.)

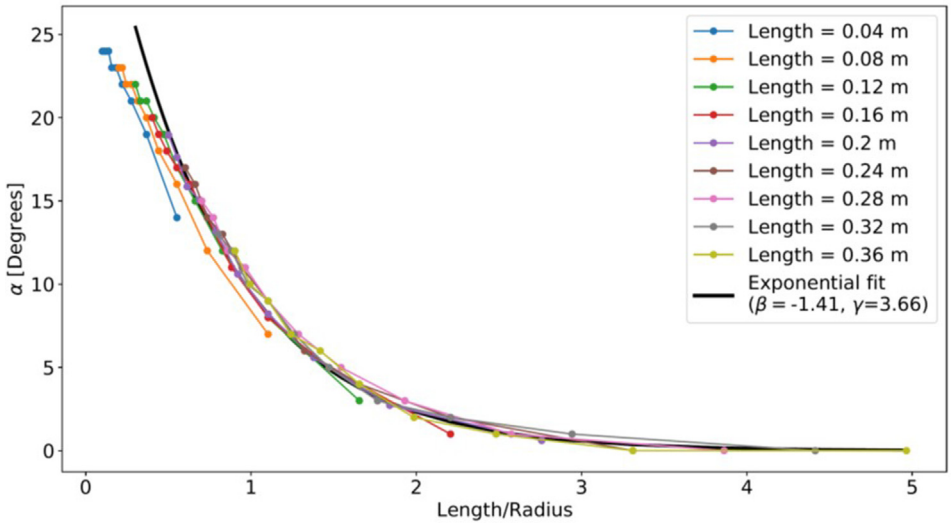

Fig. 3. Plot of the coefficient α which produces maximum homogeneity as a function of the L/R. An empirical exponential fit is shown by the black solid line.

Based upon the general shape of the plots shown in Fig. 3, an empirical exponential function was fitted to the value of α which gives the following expression:

$$\alpha = e^{-\left(\beta\frac{L}{R}+\gamma\right)} \quad [7]$$

where L and R are the length and radius of the array. The best fit corresponds to values of β = 1.41 and γ = –3.66. As is clear from Fig. 2, the fit does not work at very low values of L/R, which is primarily due to the fact that a fraction of the spherical ROI lies outside of the array. It should be noted that the choice of an exponential function is purely empirical, which reflects the effect of the α-coefficients decreasing very rapidly at higher length/radius ratios, and the α-coefficient asymptotically approaching zero in the case of infinite length cylinders.

Fig. 4 (a) shows that the difference in inhomogeneity (*I*) values between the conventional Halbach geometry and that with optimized α increases exponentially as the L/R decreases. Expressing it as a percentage increase in field-homogeneity as in Fig. 4(b) shows that the values can be up to 17% higher for small *L/R* ratios and decreases approximately linearly for larger L/R.

The second configuration studied was a variable-diameter Halbach array, in which the diameters of the individual magnet rings are varied to achieve a more homogeneous field. For this, a variable-bore Halbach magnet was generated using a genetic algorithm as described by O'Reilly *et al.* [26,27], but using only one layer of magnets unlike in [27]. Overall there are 23 rings with a minimum ring radius constraint set to 148 mm, as depicted in Fig. 5(a): ring positions, ring diameters and number of magnets in each ring are listed in Table 1.

For the optimization simulation, random values of α were assigned to each ring in this variable-diameter design at the start. The previously-described random-search algorithm then looked for the optimum array of α values which provides the lowest inhomogeneity. Symmetry was enforced with respect to the z = 0 plane along the major axis. Table 1 shows the optimum α values for each individual ring. The modified Halbach configuration provided an

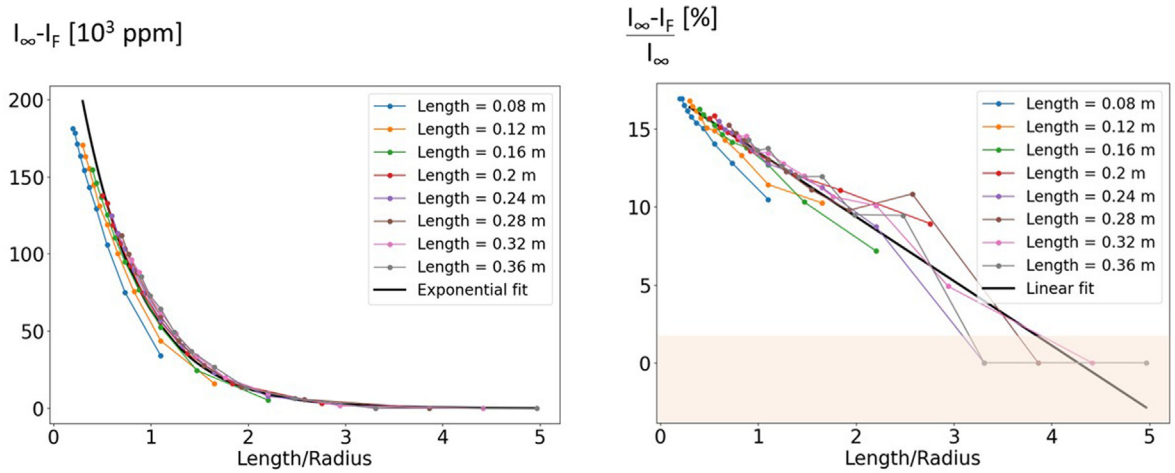

Fig. 4. (a) Improvement in the field homogeneity values (in ppm) are plotted as a function of L/R. The black solid line shows an empirical exponential fit. I_F is the homogeneity of the finite length array and I_∞ that of the infinitely long array. (b) Data normalized to the homogeneity value obtained for an infinite length Halbach cylinder. The normalized curve shows a linear drop with L/R value. The orange shaded-region at the bottom shows the noise-limit due to finite simulation resolution. (For interpretation of the references to colour in this figure legend, the reader is referred to the web version of this article.)

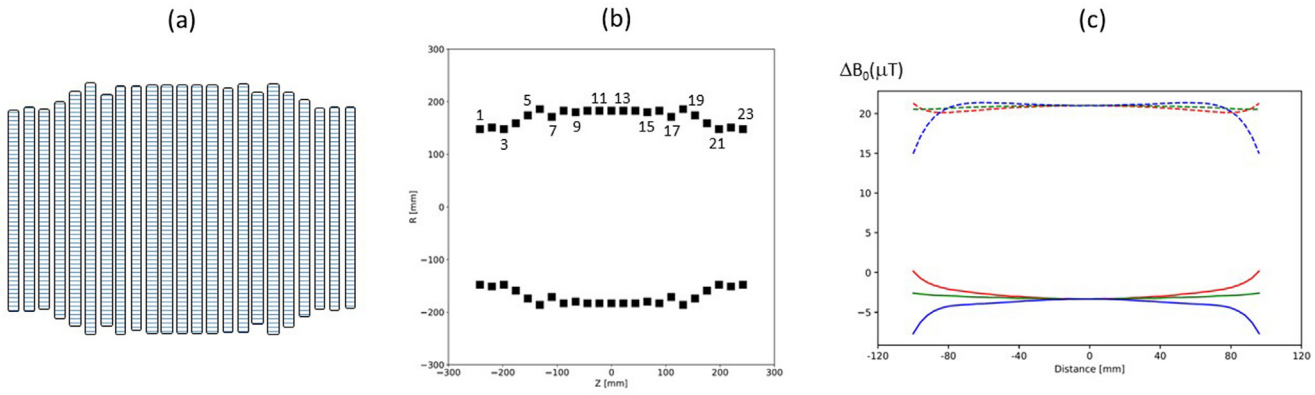

Fig. 5. (a) and (b) Schematics showing the cross-sections of the 23 ring variable-diameter Halbach array, with values of the radii listed in Table 1. (b) Magnetic field plotted along the x-(red), y-(green), and z-(blue) axes for the initial state (solid line) and final state (dotted line) after optimization: the reference for the $\triangle B_0$ is 28.3 mT which is the mean magnetic field within the 20 cm DSV for the initial state. (For interpretation of the references to colour in this figure legend, the reader is referred to the web version of this article.)

Table 1
Optimized α values for variable diameter Halbach array.

	Z (mm)	R (mm)	No.magnets	α
Ring 1	−242	148	50	−4.8
Ring 2	−220	151	51	−4.7
Ring 3	−198	148	50	2.4
Ring 4	−176	159	54	−1.5
Ring 5	−154	174	59	1.8
Ring 6	−132	186	63	0.6
Ring 7	−110	171	58	0.8
Ring 8	−88	183	62	−1.5
Ring 9	−66	180	61	−0.1
Ring 10	−44	183	62	0.5
Ring 11	−22	183	62	0.1
Ring 12	0	183	62	−0.4
Ring 13	22	183	62	0.1
Ring 14	44	183	62	0.5
Ring 15	66	180	61	−0.1
Ring 16	88	183	61	−1.5
Ring 17	110	171	58	0.8
Ring 18	132	186	63	0.6
Ring 19	154	174	59	1.8
Ring 20	176	159	54	−1.5
Ring 21	198	148	50	2.4
Ring 22	220	151	51	−4.7
Ring 23	242	148	50	−4.8

18% improvement in homogeneity, and a very slight increase in magnetic field, as shown in Fig. 5(c).

4. Discussion

Low-field MRI using either electromagnets or permanent magnets has seen a recent upsurge in interest, with applications in resource-limited environments being one of the specific targets [32–34]. Many permanent magnet designs have been put forward, including two large discs arranged with a vertical gap in-between [35,36], various forms of ring-pairs [37], and most commonly Halbach arrays: a detailed review article has been published recently [38]. For NMR studies using Halbach arrays, the length of the magnet can often be much larger than the diameter, which results in a very homogeneous main field distribution by using the classic azimuthal arrangement of magnetization vectors: however, in order to have practical dimensions for portable MRI applications the length-to-radius ratio is reduced considerably, which reduces the homogeneity.

Interesingly, Mḥıocháin et al. [10] showed that, due to end-effects, the field generated by the Halbach array along the main-field direction has additional cos(2θ) perturbations over the mean homogeneous-field component. The coefficient ($\triangle$H) of this perturbation can be expanded up to the third order and written as following in terms of the L/R:

$$\Delta H = sin^4\left(\frac{1}{\sqrt{\frac{1}{4}\left(\frac{L}{R}\right)^2+1}}\right)cos\left(\frac{\frac{1}{2}\frac{L}{R}}{\sqrt{\frac{1}{4}\left(\frac{L}{R}\right)^2+1}}\right) \quad [8]$$

Fig. 6 shows a plot of this ΔH term. The qualitative resemblance of this with the α term variation shown in Fig. 3 suggests that the changes in magnet angular orientation may be at least partially counterbalancing these field perturbations.

All of the simulation results must ultimately be put in the context of manufacturing tolerances in the positioning of the discrete magnets [17], as well as variations in the intrinsic internal orientation of the magnetic field and its magnitude. Certainly from Table 1 differences in less than 1° may prove difficult to execute unless extremely precise machining is available. Along these lines we note that a similar compensation can be achieved by using variable strength magnets with a cos(2θ) dependence in the magnet strength. Given the manufacturing tolerances mentioned above, this might be a more practical way of maximizing homogeneity. Individual magnets can potentially be sorted into bins of similar internal orientation or magnitude, and variations in internal orientation used to adjust the exact positioning. In this work we have

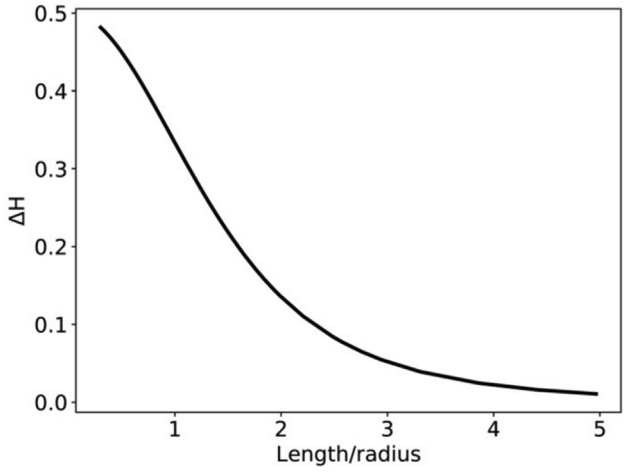

Fig. 6. Plot of the $\triangle$H coefficent of the cos(2θ) field perturbation term in the article by Mhiochain et al. [10], as a function of L/R.

also used magnet sizes and strengths which are readily commercially available, and arrangements which are practical from a manufacturing point-of-view. If one has the ability to manufacture magnets of arbitrary sizes and geometries, then optimization would undoubtedly result in higher levels of homogeneity than those achieved here, and also higher absolute field strengths if magnet geometries with higher "filling factors" can be produced, for example by using octagonal rather than cubic magnets.

5. Conclusion

In this work we perform simulations, the results of which indicate that by optimizing the orientations of individual magnets in each ring of a Halbach array, improvements in magnet homogeneity compared to the conventional 2θ orientations can be obtained, with these improvements being largest for low values of L/R where the problem is greatest. The changes to the angular orientations fitted very well to a cosinusoidal function, with the magnitude of this perturbation increasing exponentially (empirically determined) as the ratio decreases. Furthermore we have shown that the same cos (2θ) dependence holds for finite-size variable-diameter Halbach arrays. The explicit expression derived for the magnetization orientation for finite-size Halbach systems allows one to find optimum magnetization orientation without requiring advanced search-algorithms as it decreases the number of free-parameters to two.

Declaration of Competing Interest

The authors declare that they have no known competing financial interests or personal relationships that could have appeared to influence the work reported in this paper.

Acknowledgements

This work was supported by Horizon 2020 European Research Grant FET-OPEN 737180 Histo MRI, Horizon 2020 ERC Advanced NOMA-MRI 670629, Simon Stevin Meester Prize and NWO WOTRO Joint SDG Research Programme W 07.303.101.

Appendix A. Supplementary data

Supplementary data to this article can be found online at https://doi.org/10.1016/j.jmr.2021.106923.

References

[1] J.C. Mallinson, One-Sided Fluxes - Magnetic Curiosity, IEEE T Magn. 4 (1973) 678–682.
[2] K. Halbach, Design of Permanent Multipole Magnets with Oriented Rare-Earth Cobalt Material, Nucl. Instrum. Meth. 169 (1) (1980) 1–10.
[3] K. Halbach, Strong Rare-Earth Cobalt Quadrupoles, B Am. Phys. Soc. 24 (2) (1979) 183.
[4] K. Halbach, Perturbation Effects in Segmented Rare-Earth Cobalt Multipole Magnets, Nucl. Instrum. Meth. Phys. Res. 198 (2–3) (1982) 213–215.
[5] Z.Q. Zhu, D. Howe, Halbach permanent magnet machines and applications: a review, IEEE Proceed.-Electric Power Appl. 148 (4) (2001) 299–308.
[6] P.V. Trevizoli, J.A. Lozano, G.F. Peixer, J.R. Barbosa, Design of nested Halbach cylinder arrays for magnetic refrigeration applications, J. Magn. Magn. Mater. 395 (2015) 109–122.
[7] Y.J. Wang, C.D. Chen, C.K. Sung, C. Li, Natural frequency self-tuning energy harvester using a circular Halbach array magnetic disk, J. Intel. Mat. Syst. Str. 23 (8) (2012) 933–943.
[8] G. Brown, K. Halbach, J. Harris, H. Winick, Wiggler and Undulator Magnets - a Review, Nucl. Instrum. Methods Phys. Res. 208 (1–3) (1983) 65–77.
[9] J.E. Hilton, S.M. McMurry, Halbach cylinders with improved field homogeneity and tailored gradient fields, IEEE T Magn. 43 (5) (2007) 1898–1902.
[10] T.R. Ni Mhiochain, D. Weaire, S.M. McMurry, J.M.D. Coey, Analysis of torque in nested magnetic cylinders, J. Appl. Phys. 86 (11) (1999) 6412–6424.
[11] K. Turek, P. Liszkowski, Magnetic field homogeneity perturbations in finite Halbach dipole magnets, J. Magn. Reson. 238 (2014) 52–62.
[12] H. Raich, P. Blumler, Design and construction of a dipolar Halbach array with a homogeneous field from identical bar magnets, NMR Mandhalas. Concept Magn. Reson B 23b (1) (2004) 16–25.
[13] H. Soltner, P. Blumler, Dipolar Halbach Magnet Stacks Made from Identically Shaped Permanent Magnets for Magnetic Resonance, Concept Magn. Reson A. 36a (4) (2010) 211–222.
[14] P. Blumler, F. Casanova, Hardware developments: Halbach magnet arrays, in: Mobile NMR and MRI: Developments and Applications, Royal Society of Chemistry, Cambridge, UK, 2015, pp. 133–157.
[15] H. Zijlstra, Permanent magnet systems for NMR tomography, Philips J. Res. 40 (1985) 259–288.
[16] R. Ravaud, G. Lemarquand, Magnetic Field in Mri Yokeless Devices: Analytical Approach, Prog. Electromagn. Res. 94 (2009) 327–341.
[17] C. Hugon, F. D'Amico, G. Aubert, D. Sakellariou, Design of arbitrarily homogeneous permanent magnet systems for NMR and MRI: Theory and experimental developments of a simple portable magnet, J. Magn. Reson. 205 (1) (2010) 75–85.
[18] Q. Chen, G. Zhang, Y. Xu, X. Yang, Design and simulation of a multilayer Halbach magnet for NMR, Concept Magn. Reson B 45 (2015) 134–141.
[19] C.Z. Cooley, M.W. Haskell, S.F. Cauley, C. Sappo, C.D. Lapierre, C.G. Ha, et al., Design of Sparse Halbach Magnet Arrays for Portable MRI Using a Genetic Algorithm, IEEE T Magn. 54 (1) (2018).
[20] S. Anferova, V. Anferov, J. Arnold, E. Talnishnikh, M.A. Voda, K. Kupferschlager, et al., Improved Halbach sensor for NMR scanning of drill cores, Magn. Reson. Imaging 25 (4) (2007) 474–480.
[21] E. Danieli, J. Mauler, J. Perlo, B. Blumich, F. Casanova, Mobile sensor for high resolution NMR spectroscopy and imaging, J. Magn. Reson. 198 (1) (2009) 80–87.
[22] E. Danieli, J. Perlo, B. Blumich, F. Casanova, Highly Stable and Finely Tuned Magnetic Fields Generated by Permanent Magnet Assemblies, Phys. Rev. Lett. 110 (18) (2013).
[23] Cooley CZ, McDaniel P, Stockmann J, Srinivas SA, Cauley SF, Sliwiak M, et al. A portable brain MRI scanner for underserved settings and point-of-care imaging. arXiv:200413183 [eessIV]. 2020.
[24] C.Z. Cooley, J.P. Stockmann, B.D. Armstrong, M. Sarracanie, M.H. Lev, M.S. Rosen, et al., Two-dimensional imaging in a lightweight portable MRI scanner without gradient coils, Magn. Reson. Med. 73 (2) (2015) 872–883.
[25] J.Z. Chen, C.Y. Xu, Design and analysis of the novel test tube magnet as a device for portable nuclear magnetic resonance, IEEE Trans. Magnet. 43 (9) (2007) 3555–3557.
[26] T. O'Reilly, W.M. Teeuwisse, D. de Gans, K. Koolstra, A.G. Webb, In vivo 3D brain and extremity MRI at 50 mT using a permanent magnet Halbach array, Magn. Reson. Med. (2020).
[27] T. O'Reilly, W.M. Teeuwisse, A.G. Webb, Three-dimensional MRI in a homogenous 27 cm diameter bore Halbach array magnet, J. Magn. Reson. 307 (2019).
[28] J.X. Hu, H. Yi, Q.F. Yin, X.L. Zhou, R.S. Lu, Z.H. Ni, Design of a multilayer Halbach permanent magnet for human finger NMR detection, Int. J. Appl. Electrom. 54 (3) (2017) 315–327.
[29] G. Kustler, Computation of NdFeB-Halbach Cylinders With Circular and Elliptical Cross Sections in Three Dimensions, IEEE T Magn. 46 (9) (2010) 3601–3607.
[30] A.J. Petruska, J.J. Abbott, Optimal Permanent-Magnet Geometries for Dipole Field Approximation, IEEE T Magn. 49 (2) (2013) 811–819.
[31] R. Engel-Herbert, T. Hesjedal, Calculation of the magnetic stray field of a uniaxial magnetic domain, J. Appl. Phys. 97 (7) (2005).
[32] Sarracanie M, Salameh N. Low-Field MRI: How Low Can We Go? A Fresh View on an Old Debate. Front Phys-Lausanne. 2020;8.
[33] Bhat SS, Fernandes TT, Poojar P, da Silva Ferreira M, Rao PC, Hanumantharaju MC, et al. Low-Field MRI of Stroke: Challenges and Opportunities. J Magn Reson Imaging. 2020:e27324.
[34] L.L. Wald, P.C. McDaniel, T. Witzel, J.P. Stockmann, C.Z. Cooley, Low-cost and portable MRI, J. Magn. Reson. Imaging (2019).
[35] K.N. Sheth, M.H. Mazurek, M.M. Yuen, B.A. Cahn, J.T. Shah, A. Ward, et al., Assessment of Brai.n Injury Using Portable, Low-Field Magnetic Resonance Imaging at the Bedside of Critically Ill Patients, Jama. Neurol. (2020).
[36] He Y, He W, Tan L, Chen F, F. M, Feng H, et al. Use of 2.1 MHz MRI scanner for brain imaging and its preliminary results in stroke. J Magn Reson. 2020;319:106829.
[37] Z.H. Ren, W.C. Mu, S.Y. Huang, Design and Optimization of a Ring-Pair Permanent Magnet Array for Head Imaging in a Low-Field Portable MRI System, Ieee T Magn. 55 (1) (2019).
[38] Huang SY, Ren ZH, Obruchkov S, Gong J, Dijkstra R, Yu W. Portable Low-cost MRI System based on Permanent Magnets/Magnet Arrays. arXiv:181210474. 2018.